The 2010 Mw 8.8 Chile earthquake: Triggering on multiple segments and frequency-dependent rupture behavior

Eric Kiser[1] and Miaki Ishii[1]

Received 15 February 2011; accepted 22 February 2011; published 12 April 2011.

[1] Multi-frequency back-projection results of the February 27, 2010, Mw 8.8 Chile earthquake reveal that this earthquake consists of distinct subevents with different slip characteristics. The subevent south of the epicenter releases its energy at low frequencies (0.05–0.1 Hz), implying slow slip, and has a rupture speed around 0.8 km/s. Two subevents north of the epicenter are characterized by high-frequency energy (1–5 Hz) release. The first of these subevents appears to trigger slip on the second segment to the north, which has higher amplitude energy release and a fast propagation speed of about 2.9 km/s. In addition to these rupture details, high-frequency energy release is observed at the rupture front followed by lower-frequency energy release. This observation suggests that the rupture of large earthquakes involves dynamic weakening of faults and hence their rupture properties may not be related easily to those of small earthquakes. These distinct slip behaviors point out the need to consider data from a wide range of frequencies to fully assess the rupture process and associated hazards of giant earthquakes. **Citation:** Kiser, E., and M. Ishii (2011), The 2010 Mw 8.8 Chile earthquake: Triggering on multiple segments and frequency-dependent rupture behavior, *Geophys. Res. Lett.*, *38*, L07301, doi:10.1029/2011GL047140.

1. Introduction

[2] The February 27, 2010 Mw 8.8 Maule, Chile earthquake was the fifth largest event to occur in the past century. While the aftershock distribution for this event suggests a rupture length of 600 to 650 km, there is a wide range of finite fault models with highly variable slip distributions [e.g., *Delouis et al.*, 2010; *Lay et al.*, 2010; *Moreno et al.*, 2010]. For example, a seismological study by *Lay et al.* [2010] finds that the highest slip occurred north of the epicenter, southwest of Santiago, which agrees with many of the finite-fault modelling studies that use seismic data [e.g., *Delouis et al.*, 2010]. In contrast, the horizontal displacement measured by GPS stations (http://sopac.ucsd.edu/dataArchive/) is 25 times larger at Concepción (south of the epicenter) than at Santiago (north of the epicenter) (Figure 1a). A slip inversion using GPS data confirms that this displacement requires much more slip near Concepción than north of the epicenter [e.g., *Moreno et al.*, 2010].

[3] To help resolve this discrepancy, we study the rupture properties of the Chilean event using a modified back-projection technique [*Ishii et al.*, 2005; *Ishii et al.*, 2007; E. Kiser and M. Ishii, Combining seismic arrays to image the behaviour of large earthquakes at high frequencies, in prep] (see auxiliary material) applied to data from the Full Range Seismograph Network (F-net) [*Okada et al.*, 2004] and the High Sensitivity Seismograph Network (Hi-net) [*Okada et al.*, 2004; *Obara et al.*, 2005] of Japan and the Transportable Array (TA) in the United States (Figure 1b).[1] The waveform of the first-arriving compressional wave recorded on the vertical component is used at each array. In order to investigate the frequency dependence of the Chilean event, the data are bandpass-filtered to three frequency ranges, 1 to 5 Hz, 0.5 to 1 Hz, and 0.05 to 0.1 Hz, henceforth referred to as high-frequency, intermediate-frequency, and low-frequency, respectively (Figure S1). For the high- and intermediate-frequency results, spatial resolution comes mainly from the TA data, therefore we will only show these results (Figure S2). However, as we discuss later, the Hi-net data are vital in confirming some of the features observed in the TA results. For the low-frequency results, the F-net and TA data are combined to improve resolution (Figure S2).

2. Segmentation

[4] Back-projection results using high-frequency data reveal that this event is composed of three rupture segments defined by different rupture velocities and amplitudes (Figure 2 and Animation S1). Segment 1 is a north/south bilateral rupture (between about 36.5°S and 36°S) away from the epicenter, though the northward propagating rupture has higher amplitude energy release. This northward rupture lasts about 45 seconds and has a velocity of about 2.2 km/s (Figure 2 and Animation S2). North of Segment 1 is Segment 2 (between about 35°S and 34°S), which has the highest amplitude energy release of all the segments at high frequency. It begins to rupture about 55 seconds after the hypocentral time, and propagates to the northeast for 60 seconds with a distinctly higher rupture velocity of around 2.9 km/s (Figure 2 and Animation S1). In contrast, Segment 3 is located south of the epicenter at about 37.5°S, and is activated 70 seconds after the hypocentral time. This segment ruptures for 25 seconds at a rupture velocity of 0.8 km/s to the east, and has the weakest energy release of all the segments at high frequency (Figure 2 and Animation S3). Note that the weak southern rupture of Segment 1 is obscured by the energy from the strong northern rupture, and therefore we cannot determine the rupture parameters that connect Segments 1 and 3. However, if we assume a continuous southern rupture, the rupture speed required between the epicenter and the initiation of Segment 3

[1]Department of Earth and Planetary Sciences, Harvard University, Cambridge, Massachusetts, USA.

0094-8276/11/2011GL047140

[1]Auxiliary materials are available in the HMTL. doi:10.1029/2011GL047140.

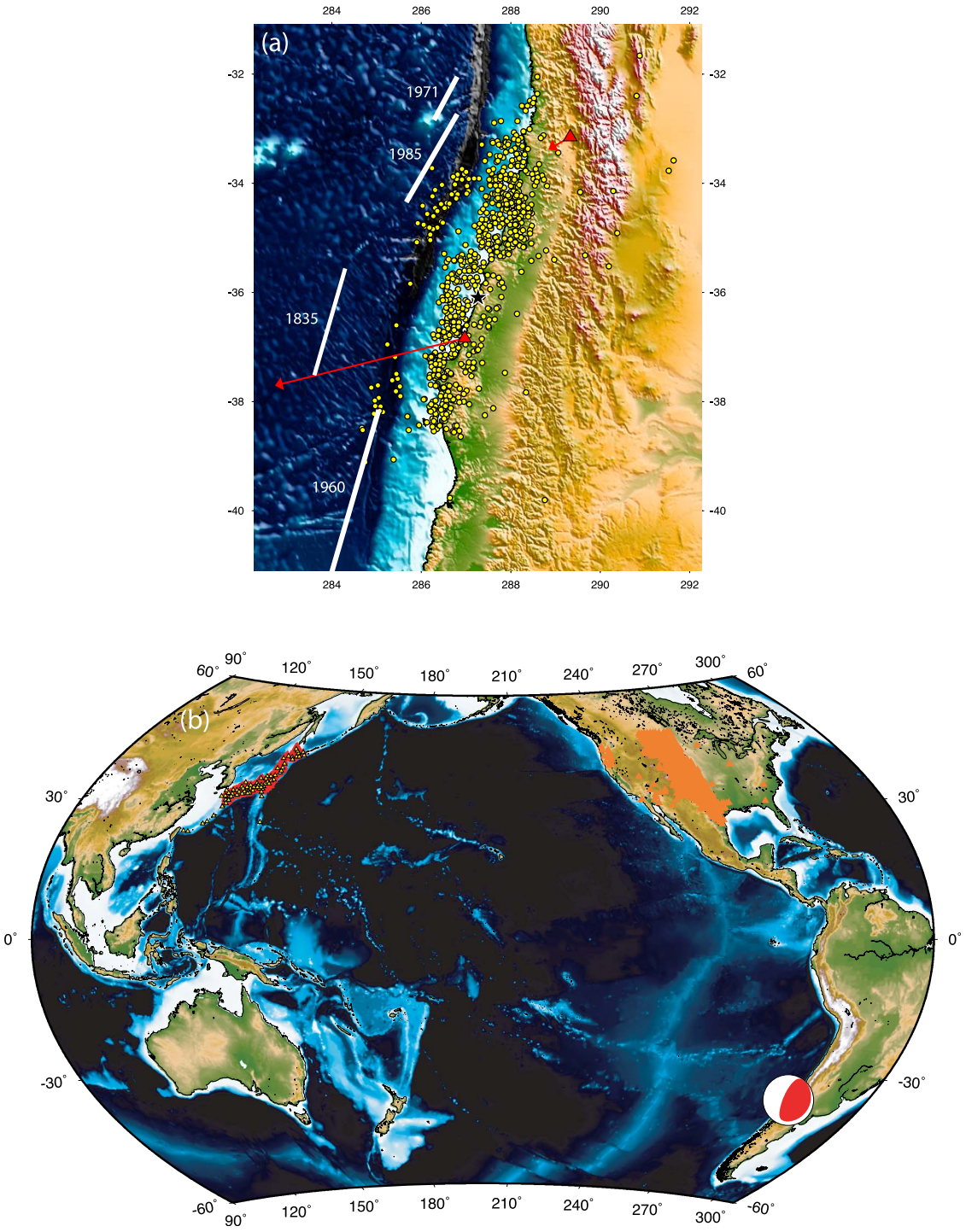

Figure 1. Earthquake overview. (a) The epicenter (black star) and aftershock distribution (yellow circles) of the 2010 Chile event 3 months following the mainshock. These locations are from the USGS National Earthquake Information Center (http://earthquake.usgs.gov/). The red triangles are the GPS stations that recorded the horizontal displacement (red vectors) one day after the event near Santiago (0.8 cm) and Concepción (20 cm) provided by the Scripps Orbit and Permanent Array Center (http://sopac.ucsd.edu/). The white lines show the approximate latitudinal extents of recent large earthquakes in this region [e.g., *Beck et al.*, 1998]. (b) TA (orange triangles), Hi-net (red triangles) and F-net (small yellow triangles) station distributions relative to the focal mechanism of the February 27, 2010 Chile earthquake from the Global CMT catalog [e.g., *Dziewonski and Woodhouse*, 1983; *Dziewonski et al.*, 1981]. In order to avoid the triplication of the core phases, only a subset of the Hi-net stations with distances between 150 and 153 degrees are used.

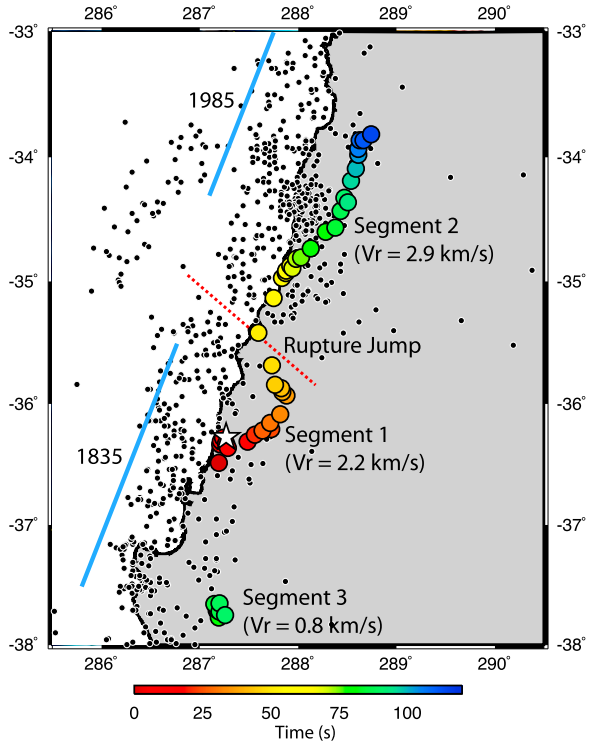

Figure 2. Locations of peak energy release as a function of time. The large colored circles show the locations of imaged energy using high-frequency (1–5 Hz) TA data with the colors indicating the corresponding times with respect to the hypocentral time. The white star is the hypocenter and the small black dots are the aftershocks. The labels indicate the three different rupture velocities (Vr) associated with this event and the northwest jump in the rupture between Segments 1 and 2. The dashed red line marks the gap in the aftershock distribution that corresponds to the change in rupture characteristics (i.e., a change in rupture velocity) and the interseismic coupling of the subduction zone [*Moreno et al.*, 2010]. The light blue lines show the approximate latitudinal extents of the most relevant large earthquakes in this region [e.g., *Beck et al.*, 1998].

is 2.2 km/s to the south, implying a dramatic decrease in rupture velocity and change in rupture direction at Segment 3.

[5] This segmentation of the slab interface is corroborated by historical seismicity of the region (Figure 2). The latitudinal extent of Segment 2 is consistent with the inferred rupture zone of the 1985 Mw 8.0 Valparaiso earthquake [e.g., *Christensen and Ruff*, 1986; *Beck et al.*, 1998], and Segments 1 and 3 occur at the northern and southern regions, respectively, of the seismic gap between the 1985 and 1960 Chilean earthquakes, which has not slipped since the 1835 Darwin event (Figure 2) [e.g., *Barrientos and Ward*, 1990; *Beck et al.*, 1998]. In addition, the boundary between Segments 1 and 2 coincides with a region of low interseismic coupling as inferred by continuous GPS data [*Moreno et al.*, 2010]. The northern and southern extents of the 2010 earthquake have been argued to be controlled by visible surface features, i.e., the Juan Fernandez Ridge and the Mocha Fracture Zone [e.g., *von Huene et al.*, 1997; *Contreras-Reyes et al.*, 2008], but results presented here also indicate that regions of low interseismic coupling can act to segment a rupture. As discussed later, this segmentation may have important consequences for the hazards associated with large earthquakes.

3. Triggering

[6] There is a noticeable jump in the imaged high-frequency energy release as it moves from Segment 1 to 2 at about 35°S (Figure 2 and Animation S2). This jump involves a 75 km gap in the imaged rupture, which lasts for 10 seconds between 45 and 55 seconds after the hypocentral time. If this "gap" is due to very weak rupture, the required propagation or rupture speed is 7.5 km/s, which is close to the *P* wave speed [e.g., *Kennett and Engdahl*, 1991]. This observation suggests that slip on Segment 1 stopped at about 35°S and dynamically triggered slip on Segment 2. The spatial gap is also seen in the aftershock distribution where a break in aftershock activity exists between Segments 1 and 2 (Figure 2), supporting the interpretation that no coseismic slip occurred in this narrow region.

4. Frequency-Dependent Energy Release

[7] We next investigate the frequency-dependent properties of each segment identified in the previous section using the three bandpass-filtered data. Figures 3a and 3b show that the high-frequency energy is radiated at the rupture front while the intermediate-frequency energy lags behind for Segments 1 and 2 (Animations S4 and S5). The frequency-dependent characteristics of Segment 3 are slightly different than those of Segments 1 and 2. Both the high- and intermediate-frequency results are dominated by a single episode of energy release with slow propagation velocities. This slow speed, in the presence of imperfect spatial resolution, makes tracking of the energy at two frequencies difficult. However, the peak of the high-frequency energy is farther south than the intermediate-frequency energy (Figure 3c and Animation S6). These observations from all three segments can be interpreted as "breaking" of the fault at the rupture tip, releasing high-frequency energy, followed by slower slip behind the rupture front due to reduced friction. These types of rupture dynamics, which point to the importance of dynamic weakening of faults, have been proposed theoretically [e.g., *McKenzie and Brune*, 1972; *Sibson*, 1973, 1977; *Richards*, 1976; *Lachenbruch*, 1980; *Mase and Smith*, 1987; *Melosh*, 1996; *Kanamori and Heaton*, 2000; *Brodsky and Kanamori*, 2001; *Rempel and Rice*, 2006; *Rice*, 2006] and observed both experimentally [e.g., *Di Toro et al.*, 2004; *Han et al.*, 2007; *Hirose and Bystricky*, 2007; *Famin et al.*, 2008; *Nielsen et al.*, 2008] and for the 1999 Chi-Chi earthquake [*Ma et al.*, 2003]. The reduction in friction caused by processes such as pore fluid thermal pressurization and frictional melt [e.g., *Rempel and Rice*, 2006; *Nielsen et al.*, 2008] requires substantial slip, and therefore this effect should not apply to small earthquakes. The observation of frequency-dependent energy release suggests that small and large subduction zone earthquakes behave differently, and that one cannot simply scale the behavior of small events to understand the occurrence and mechanism of giant earthquakes. Another interesting observation from comparing high- and intermediate-frequency results is that both the northern edge of Segment 2 and the southern edge of Segment 3 are marked by bursts of high-frequency energy release that occur after the energy release at intermediate frequencies (Animations S4 and S6). We interpret these high-frequency features as the

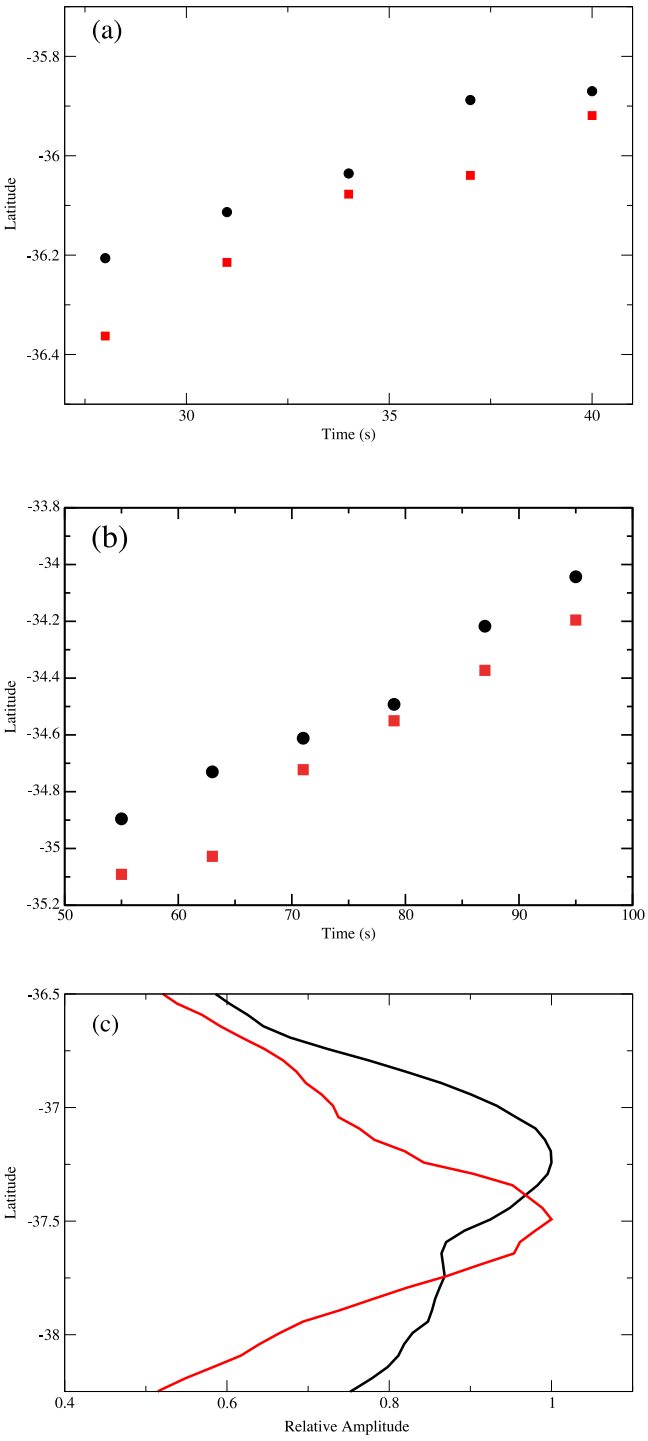

Figure 3. High- (1–5 Hz) and intermediate- (0.5–1 Hz) frequency back-projection results. (a) Latitudes and times of the imaged energy from Segment 1 using high- (1–5 Hz; black circles) and intermediate-frequency (0.5–1 Hz; red squares) TA data. (b) Latitudes and times of the imaged energy from Segment 2 using high- (1–5 Hz; black circles) and intermediate-frequency (0.5–1 Hz; red squares) TA data. (c) Relative amplitude distribution with respect to latitude of the imaged energy from Segment 3 using high- (1–5 Hz; red line) and intermediate-frequency (0.5–1 Hz; black line) TA data.

stopping phases that result from the sudden decrease in rupture velocity as the ruptures terminate [*Savage*, 1966].

[8] The poor spatial resolution of low-frequency back-projection results makes it difficult to determine this energy's relationship to each of the three segments identified above (Figure S2). However, there is adequate latitudinal resolution to determine that this energy peaks south of the epicenter, which is in contrast to high-frequency results where energy release prevails to the north (Figures 4 and S3). These results are confirmed with back-projection results using high-frequency data from Hi-net and low-frequency data from TA and F-net, individually (Figure S4), and are not the result of the directivity effect (for more detailed discussion, see auxiliary material). This difference in frequency content suggests that the dynamics of slip change along the subduction zone during a single giant earthquake. Note that high-frequency energy release is largest on Segment 2 north of the epicenter where the rupture speed is high (2.9 km/s) and low-frequency energy release is largest near Segment 3 south of the epicenter where the rupture speed is low (0.8 km/s). This relationship between rupture speed and relative energy release at different frequencies suggests that the rupture velocity scales with the rise-time of slip [*Aki and Richards*,

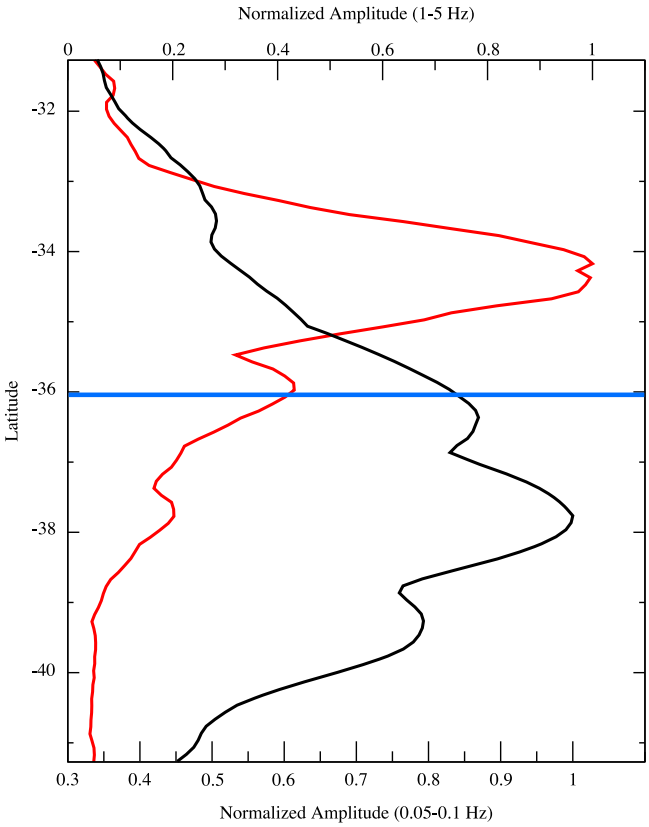

Figure 4. Northern and southern segments of the 2010 Chilean earthquake. The relative amplitude variation of high- (1–5 Hz; red line) and low-frequency (0.05–0.1 Hz; black line) stacks as a function of latitude. The blue line is the epicentral latitude. The separation of the northern high-frequency rupture and the southern low-frequency rupture points out that this rupture took place on two mechanically different faults.

2002]. It can therefore be interpreted that Segments 1 and 2 slipped fast while Segment 3 had slower slip.

5. Discussion and Conclusions

[9] This study shows that a giant earthquake can involve distinct segments of a slab interface and that different frequency ranges need to be considered to fully assess the complexity of these events. One consequence of the frequency-dependent slip behavior is the tsunami generation potential of the earthquake. Tsunamis are known to be more effectively excited by sources involving long-period or low-frequency deformation [*Kanamori*, 1972]. For example, based upon our observation, the region to the south of, and around the epicenter, has higher tsunami potential than that to the north, despite large slip seen to the north in most of the finite-fault or back-projection results. This simple interpretation may not fully characterize the tsunami potential given the fact that the distance of slip from the trench varies during the rupture and our "low" frequency may still be relatively high for efficient deformation. However, it does point out that tsunami wave modeling for early warning may need to incorporate frequency-dependent source complexity for giant earthquakes. A second consequence of this study comes from the fact that damage to structures is also frequency dependent [*Stein and Wysession*, 2003]. This implies that studies that estimate strong motion and hazard for the purpose of resource allocation of the emergency earthquake response should consider where slip at relevant frequencies is occurring. Finally, the frequency dependence of the energy release distribution presented in this paper provides a possible mechanism to resolve the discrepancy between slip models that use seismological and geodetic data. For example, the limited strain release on the northern segments observed for the 2010 Chilean event suggests that the slip mechanism that releases seismic energy predominantly at high-frequency does not release strain efficiently. This implies that events with slip with high-frequency energy release do not necessarily reset the recurrence time to the next big earthquake. Similarly, the total slip measured by GPS instruments over one or more days may not, and in the case of the 2010 Chilean earthquake, is not, equal to the distribution of slip associated with high-frequency energy release easily recorded by the first-arriving seismic waves.

[10] **Acknowledgments.** Some figures have been generated using the Generic Mapping Tools [*Wessel and Smith*, 1991]. The authors thank the National Research Institute for Earth Science and Disaster Prevention in Japan and the IRIS Data Management Center for making the F-net, Hi-net and TA data available. Discussions with Renata Dmowska and Adam Dziewonski helped to interpret results in the manuscript. This manuscript also benefited from constructive reviews by Alex Hutko and an anonymous reviewer. This project was funded by NSF EAR-0609092.

[11] The Editor thanks two anonymous reviewers for their assistance in evaluating this paper.

References

Aki, K., and P. G. Richards (2002), *Quantitative Seismology*, Univ. Sci., Sausalito, Calif.

Barrientos, S. E., and S. N. Ward (1990), The 1960 Chile earthquake: Inversion for slip distribution from surface deformation, *Geophys. J. Int.*, *103*, 589–598, doi:10.1111/j.1365-246X.1990.tb05673.x.

Beck, S., S. Barrientos, E. Kausel, and M. Reyes (1998), Source characteristics of historic earthquakes along the central Chile subduction zone, *J. South Am. Earth Sci.*, *11*, 115–129, doi:10.1016/S0895-9811(98)00005-4.

Brodsky, E. E., and H. Kanamori (2001), Elastohydrodynamic lubrication of faults, *J. Geophys. Res.*, *106*, 16,357–16,374, doi:10.1029/2001JB000430.

Christensen, D., and L. Ruff (1986), Rupture process of the March 3, 1985 Chilean earthquake, *Geophys. Res. Lett.*, *13*, 721–724, doi:10.1029/GL013i008p00721.

Contreras-Reyes, E., I. Grevemeyer, E. R. Flueh, and C. Reichert (2008), Upper lithospheric structure of the subduction zone offshore of southern Arauco peninsula, Chile, at 38°S, *J. Geophys. Res.*, *113*, B07303, doi:10.1029/2007JB005569.

Delouis, B., J.-M. Nocquet, and M. Vallee (2010), Slip distribution of the February 27, 2010 Mw = 8.8 Maule earthquake, central Chile, from static and high-rate GPS, InSAR, and broadband teleseismic data, *Geophys. Res. Lett.*, *37*, L17305, doi:10.1029/2010GL043899.

Di Toro, G., D. L. Goldsby, and T. E. Tullis (2004), Friction falls towards zero in quartz rock as slip velocity approaches seismic rates, *Nature*, *427*, 436–439, doi:10.1038/nature02249.

Dziewonski, A. M., and J. H. Woodhouse (1983), An experiment in systematic study of global seismicity: Centroid-moment tensor solutions for 201 moderate and large earthquakes of 1981, *J. Geophys. Res.*, *88*, 3247–3271, doi:10.1029/JB088iB04p03247.

Dziewonski, A. M., T. A. Chou, and J. H. Woodhouse (1981), Determination of earthquake source parameters from waveform data for studies of global and regional seismicity, *J. Geophys. Res.*, *86*, 2825–2852, doi:10.1029/JB086iB04p02825.

Famin, V., S. Nakashima, A. M. Boullier, K. Fujimoto, and T. Hirono (2008), Earthquakes produce carbon dioxide in crustal faults, *Earth Planet. Sci. Lett.*, *265*(3–4), 487–497, doi:10.1016/j.epsl.2007.10.041.

Han, R., T. Shimamoto, T. Hirose, J.-H. Ree, and J. Ando (2007), Ultralow friction of carbonate faults caused by thermal decomposition, *Science*, *316*, 878–881, doi:10.1126/science.1139763.

Hirose, T., and M. Bystricky (2007), Extreme weakening of faults during dehydration by coseismic shear heating, *Geophys. Res. Lett.*, *34*, L14311, doi:10.1029/2007GL030049.

Ishii, M., P. M. Shearer, H. Houston, and J. E. Vidale (2005), Extent, duration and speed of the 2004 Sumatra-Andaman earthquake imaged by the Hi-net array, *Nature*, *435*, 933–936.

Ishii, M., P. M. Shearer, H. Houston, and J. E. Vidale (2007), Teleseismic P wave imaging of the 26 December 2004 Sumatra-Andaman and 28 March 2005 Sumatra earthquake ruptures using the Hi-net array, *J. Geophys. Res.*, *112*, B11307, doi:10.1029/2006JB004700.

Kanamori, H. (1972), Mechanism of tsunami earthquakes, *Phys. Earth Planet. Inter.*, *6*, 346–359, doi:10.1016/0031-9201(72)90058-1.

Kanamori, H., and T. H. Heaton (2000), Microscopic and macroscopic physics of earthquakes, *U.S. Geol. Surv. Open File Rep.*, *OF 00-0129*, 41 pp.

Kennett, B. L. N., and E. R. Engdahl (1991), Traveltimes for global earthquake location and phase identification, *Geophys. J. Int.*, *105*, 429–465, doi:10.1111/j.1365-246X.1991.tb06724.x.

Lachenbruch, A. H. (1980), Frictional heating, fluid pressure, and the resistance of fault motion, *J. Geophys. Res.*, *85*, 6097–6112, doi:10.1029/JB085iB11p06097.

Lay, T., C. J. Ammon, H. Kanamori, K. D. Koper, O. Sufri, and A. R. Hutko (2010), Teleseismic inversion for rupture process of the 27 February 2010 Chile (M_w 8.8) earthquake, *Geophys. Res. Lett.*, *37*, L13301, doi:10.1029/2010GL043379.

Ma, K.-F., E. E. Brodsky, J. Mori, C. Ji, T.-R. A. Song, and H. Kanamori (2003), Evidence for fault lubrication during the 1999 Chi-Chi, Taiwan, earthquake (Mw7.6), *Geophys. Res. Lett.*, *30*(5), 1244, doi:10.1029/2002GL015380.

Mase, C. W., and L. Smith (1987), Effects of frictional heating on the thermal, hydrologic, and mechanical response of a fault, *J. Geophys. Res.*, *92*, 6249–6272, doi:10.1029/JB092iB07p06249.

McKenzie, D. P., and J. N. Brune (1972), Melting of fault planes during large earthquakes, *Geophys. J. R. Astron. Soc.*, *29*, 65–78.

Melosh, H. J. (1996), Dynamical weakening of faults by acoustic fluidization, *Nature*, *379*, 601–606, doi:10.1038/379601a0.

Moreno, M., M. Rosenau, and O. Oncken (2010), 2010 Maule earthquake slip correlates with pre-seismic locking of the Andean subduction zone, *Nature*, *467*, 198–202, doi:10.1038/nature09349.

Nielsen, S., G. Di Toro, T. Hirose, and T. Shimamoto (2008), Frictional melt and seismic slip, *J. Geophys. Res.*, *113*, B01308, doi:10.1029/2007JB005122.

Obara, K., K. Kasahara, S. Hori, and Y. Okada (2005), A densely distributed high-sensitivity seismograph network in Japan: Hi-net by National Research Institute for Earth Science and Disaster Prevention, *Rev. Sci. Instrum.*, *76*, 021301, doi:10.1063/1.1854197.

Okada, Y., K. Kasahara, S. Hori, K. Obara, S. Sekiguchi, H. Fujiwara, and A. Yamamoto (2004), Recent progress of seismic observation networks in Japan: Hi-net, F-net, K-NET and KiK-net, *Earth Planets Space*, *56*, 15–28.

Rempel, A. W., and J. R. Rice (2006), Thermal pressurization and onset of melting in fault zones, *J. Geophys. Res.*, *111*, B09314, doi:10.1029/2006JB004314.

Rice, J. R. (2006), Heating and weakening of faults during earthquake slip, *J. Geophys. Res.*, *111*, B05311, doi:10.1029/2005JB004006.

Richards, P. G. (1976), Dynamic motions near an earthquake fault: A three-dimensional solution, *Bull. Seismol. Soc. Am.*, *66*, 1–32.

Savage, J. C. (1966), Radiation from a realistic model of faulting, *Bull. Seismol. Soc. Am.*, *56*, 577–592.

Sibson, R. H. (1973), Interactions between temperature and fluid pressure during earthquake faulting and a mechanism for partial or total stress relief, *Nature*, *243*, 66–68.

Sibson, R. H. (1977), Kinetic shear resistance, fluid pressures and radiation efficiency during seismic faulting, *Pure Appl. Geophys.*, *115*, 387–400, doi:10.1007/BF01637116.

Stein, S., and M. Wysession (2003), *An Introduction to Seismology, Earthquakes, and Earth Structure*, Blackwell, Malden, Mass.

von Huene, R., J. Corvalan, E. R. Flueh, K. Hinz, J. Korstgard, C. R. Ranero, and W. Weinrebe (1997), Tectonic control of the subducting Juan Fernandez Ridge on the Andean margin near Valparaiso, Chile, *Tectonics*, *16*, 474–488, doi:10.1029/96TC03703.

Wessel, P., and W. H. F. Smith (1991), Free software helps map and display data, *Eos Trans. AGU*, *72*(41), 441, doi:10.1029/90EO00319.

M. Ishii and E. Kiser, Department of Earth and Planetary Sciences, Harvard University, 20 Oxford St., Cambridge, MA 02138, USA. (kiser@fas.harvard.edu)